Supporting Information
for

Nanoscale transforming mineral phases in fresh nacre

Ross T. DeVol[1], Chang-Yu Sun[1], Matthew A. Marcus[2], Susan N. Coppersmith[1], Satish C. B. Myneni[3], and Pupa U.P.A. Gilbert[1,4,5,*,#]

[1] Department of Physics, University of Wisconsin–Madison, 1150 University Avenue, Madison, WI 53706, USA.
[2] Advanced Light Source, Lawrence Berkeley National Laboratory, 1 Cyclotron Road, Berkeley, CA 94720, USA.
[3] Department of Geosciences, Princeton University, Princeton, NJ 08544, USA.
[4] Department of Chemistry, University of Wisconsin–Madison, 1101 University Avenue, Madison, WI 53706, USA.
[5]Radcliffe Institute for Advanced Study, Harvard University, 8 Garden Street, Cambridge, MA 02138.

*Previously publishing as Gelsomina De Stasio.
#Corresponding author: pupa@physics.wisc.edu

Methods

Live *Haliotis rufescens* (*Hr*) animals were purchased from Monterey Abalone Company, Monterey, CA, the animal was removed, and the shell was fixed either in ethanol or in 4% formaldehyde in TBST (10mM Tris base pH 11, 0.5M NaCl, 0.1% Tween 20) for 30 minutes, rinsed twice in TBST while agitating, and washed in ethanol twice, air-dried, embedded in EpoFix (EMS, Hatfield, PA), polished with 300nm, then 50nm Al_2O_3 suspension (MicroPolish and MasterPrep, respectively, Buehler, Lake Bluff, IL) dialyzed against 22 g/L Na_2CO_3 in DDH_2O, coated with 1 nm Pt in the area to be analyzed by PEEM and 40 nm around it, as described in refs. [1-4]. A 10-year-old fragment of *Madracis sp.* Coral was obtained from Satish Myneni, Princeton University. It was embedded, polished and coated as the abalone samples. SEM experiments were done at the UC-Berkeley Electron Microscopy Laboratory, using a Hitachi TM-1000 microscope, with 15 kV in backscatter electron (BSE) mode. PEEM experiments were done on PEEM-3 [5,6] at the Advanced Light Source in Berkeley, CA, USA.

Spectra were acquired by scanning the x-ray energy across the Ca L-edge, from 340 eV to 360 eV. Images were acquired at 0.5 eV intervals across the pre- and post-edge, from 340-345 and 355-360 eV, respectively, and with 0.1 eV intervals across the most interesting part of the spectrum, from 345-355 eV, for a total of 121 images. In these stacks of 121 images, termed “Ca movies”, each pixel contained the full Ca L-edge spectrum [7].

For PIC-mapping, we varied the x-ray polarization in increments of 5° from horizontal to vertical (19 images) while maintaining the photon energy constant at 534 eV, at the most polarization-sensitive oxygen K-edge π* peak, as described previously [8].

For all images the field of view was 20 μm, and the pixel size was 20 nm. The sample voltage was -18 kV, and the microscope pressure 1×10^{-8} Torr. All data processing to produce the component maps and color PIC-maps was done in Igor Pro® (WaveMetrics, Lake Oswego, OR), using Gilbert Group (GG) Macros, distributed free of charge on our web site [9].

How component spectra were obtained

Pixels in all movies and maps are 20 nm in size, thus single-pixel spectra, hereafter, are spectra extracted from a single 20-nm pixel.

The ACC-H_2O reference spectrum is the average of 39 single-pixel spectra, extracted from 4 different Ca movies (9-10 spectra per movie) of *Hr* nacre collected at the towers of fresh, forming tablets. The pixels in which the proportion of the spectrum corresponding to ACC-H_20 is largest were first identified using sea urchin spectra from Gong et al. [7], then re-run with nacre references iteratively. Finally, the spectra with greatest ACC-H_2O concentration were aligned in intensity over the full range (340 eV to 360 eV) and averaged. The resulting spectrum was then peak-fitted and scaled so its intensities are 0 and 1 at 345 eV and 355 eV, respectively, in pre- and post-edge regions of the Ca L-edge XANES spectrum.

The ACC reference spectrum is the average of 37 single-pixel spectra, extracted from 4 different movies (8-10 spectra per movie) of *Hr* nacre collected at the towers. All spectra were aligned in intensity, averaged, peak-fitted, and scaled as above.

The aragonite reference spectrum is the average of 60 single-pixel spectra, extracted from 4 different movies (15 spectra per movie) of bulk *Hr* nacre collected away from the towers. All spectra were aligned in intensity over the full range, averaged, peak-fitted, and scaled as above.

The pixels from which the reference spectra for ACC-H_2O, ACC, and aragonite were obtained were chosen via an iterative process, in which we ran component mapping and chose pixels with high proportions of the relevant component. Spectra from these pixels were then averaged and peak-fitted and used as the new reference, and the whole process was repeated several times, until we obtained the greatest possible proportions of ACC-H_2O, ACC, and aragonite: 70%, 91%, and 99.98%, respectively.

The pAra reference spectrum is the average of 157 single-pixel spectra presented in Figure S3, extracted from 4 different Ca movies (6-100 spectra

per movie) of *Madracis sp.* coral, collected at and near centers of calcification. All spectra were aligned in intensity over the range of 345 eV to 355 eV and then averaged. The resulting spectrum was then peak-fitted and scaled as above. The four peak-fitted spectra were then averaged and used as the pAra reference spectrum in Figure 1.

The reason for extracting single-pixel spectra from multiple movies, rather than a single one, is that in all spectromicroscopy experiments there is always non-statistical noise. For example, a synchrotron beam position drift due to a mirror motion, or instabilities in the synchrotron electron beam orbit, or thermal fluctuations, may generate peaks and dips at multiple energies, which are consistent across all pixels in a movie, but never consistent across different movies. Using multiple movies averaged out these small effects.

The reason for peak-fitting all averaged spectra is that some random noise still remains, which is undesirable because it interferes with the component analysis results. Peak fitting completely eliminates noise, while retaining the experimental lineshape of the spectra. The difference between the experimental spectrum and peak-fitted one, called residual, is simply random noise, as presented at the bottom of Figure S5. All averaging, peak-fitting and displaying of spectra was done using the GG macros [9]. The spectra in Figure 3 were obtained as follows: all spectra were aligned in intensity [9], a linear fit of the pre-edge was extrapolated to the entire energy range, all spectra were normalized dividing by this line, the intensity of peaks 1 and the pre-edge were set to 1 and 0, respectively, for all spectra. They were then peak-fitted with either 4 or 7 Lorentzian curves, 1 third order polynomial, and two arctangents. The arctangents were fixed in energy position at 352.5 eV and 351 eV, in width at 0.4 eV, and in amplitude at 0.04 and 0.09 for ACC-H_2O, ACC, and calcite spectra, and to 0.02 and 0.05 for aragonite and proto-aragonite. This is because the arctangent corresponding to the L_3 edge must be approximately twice as high as that of the L_2 edge [10,11]. All other parameters in Table S1 were free fit parameters. The final plots were prepared in Kaleidagraph® 4.5 for Mac, after displacing the polynomial and arctangents down, and the fit up, so that the 4 or 7 Lorentzians can clearly be distinguished in Figure 3.

Simulations of phase transitions

The simulation of Figure S7 was written in Java Eclipse Luna. There are 100 × 100 × 40 = 400,000 voxels in the simulation, forming a cuboid. Each voxel contains fractions of R, G, and B that add up to 1. When a voxel transforms from R to G, the R fraction decreases and the G fraction increases. In each time-step, each portion of R and G in a given voxel has an opportunity to transform to the next logical phase (R can go to G, G can go to B). When a transformation is fast, it has a 50% chance of transforming. When it is slow, it has only a 10% chance of transforming.

A voxel can only go from R to G if it is touching another voxel that contains G or B, and a voxel can only go from G to B if it is touching a voxel that contains B.

For all simulations, regardless of speed, no more than 30% of a given color in a given voxel can transform in any one time-step.

Two-dimensional slices were taken through the middle of the 3D cuboid volume, parallel to a side face of the cuboid. The slices are all taken after 32 time-steps, out of a total of 200 time-steps.

SI Figures and Legends

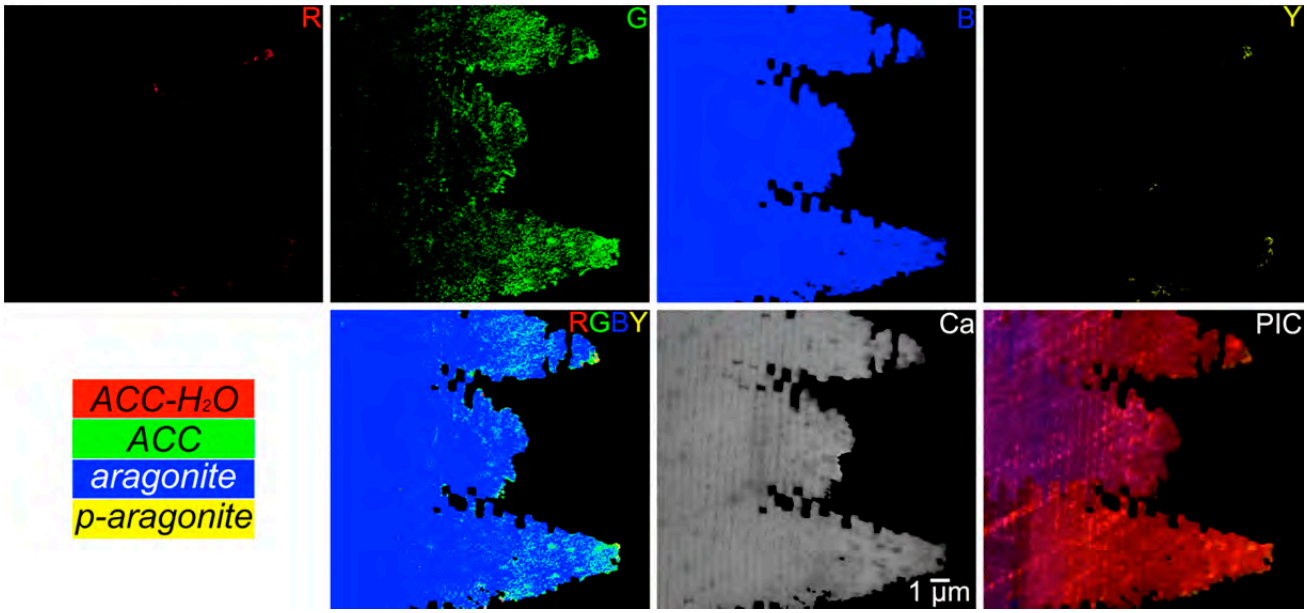

Figure S1. Distribution maps of ACC-H_2O (red, R), ACC (green, G), aragonite (blue, B), and proto-aragonite (yellow, Y). (RGBY) Component map showing the spatial distribution of all four mineral phases. (Ca) Calcium distribution map and (PIC) PIC-map of the same *Haliotis rufescens* towers as in Figure 1B in the main text, and all other panels here.

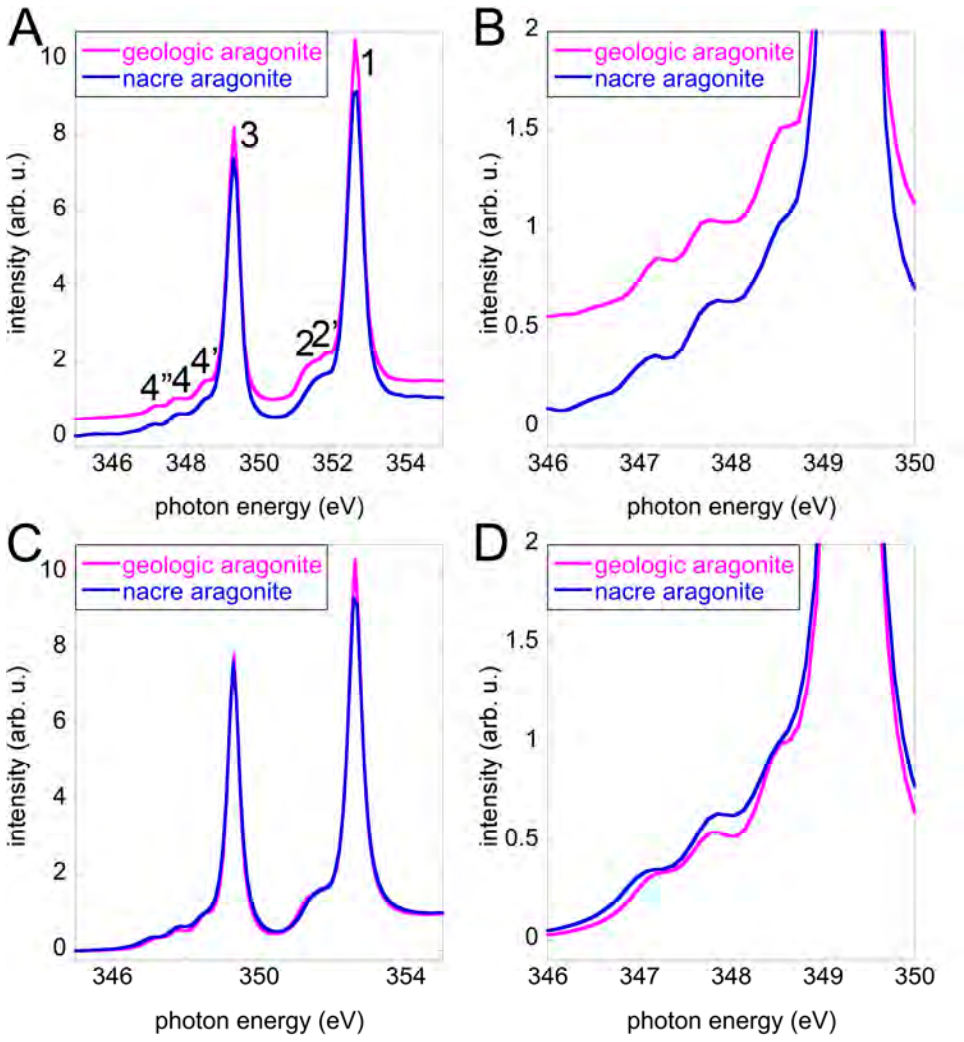

Figure S2. Comparison of Ca L-edge spectra acquired from geologic aragonite and mature nacre. (A, B) Both spectra are the average of many experimental spectra acquired over single-20nm-pixels. They are first normalized so their intensities at 345 eV and at 355 eV are 0 and 1, respectively, then they are displaced vertically for clarity. (A) The entire energy range is 340-360 eV, here we display only the most relevant 345-355 eV region. (B) Zoomed in region of the spectra in A, showing the three little peaks characteristic of aragonite (indicated in Figure 1F of the main text with blue downward arrows). No other carbonates exhibit these three little peaks. (C,D) Peak-fitted versions of the same spectra in (A) and (B), obtained with 7 Lorentzians, 1 polynomial and 2 arctangent functions, with the best-fit coefficients provided in Table S1. Here the spectra are displayed overlapping so that differences in peak width and intensity can be appreciated. Most peak intensities are comparable in nacre and geologic aragonite, only peak 1 is less intense in nacre. Most peak widths are similar, except for one of the 3 little peaks displayed in B and D: the little peak at ~348.5 eV is broader and thus less well resolved in nacre than in geo-aragonite. Both these differences indicate a slightly less ordered crystalline structure in bio- than geo-aragonite.

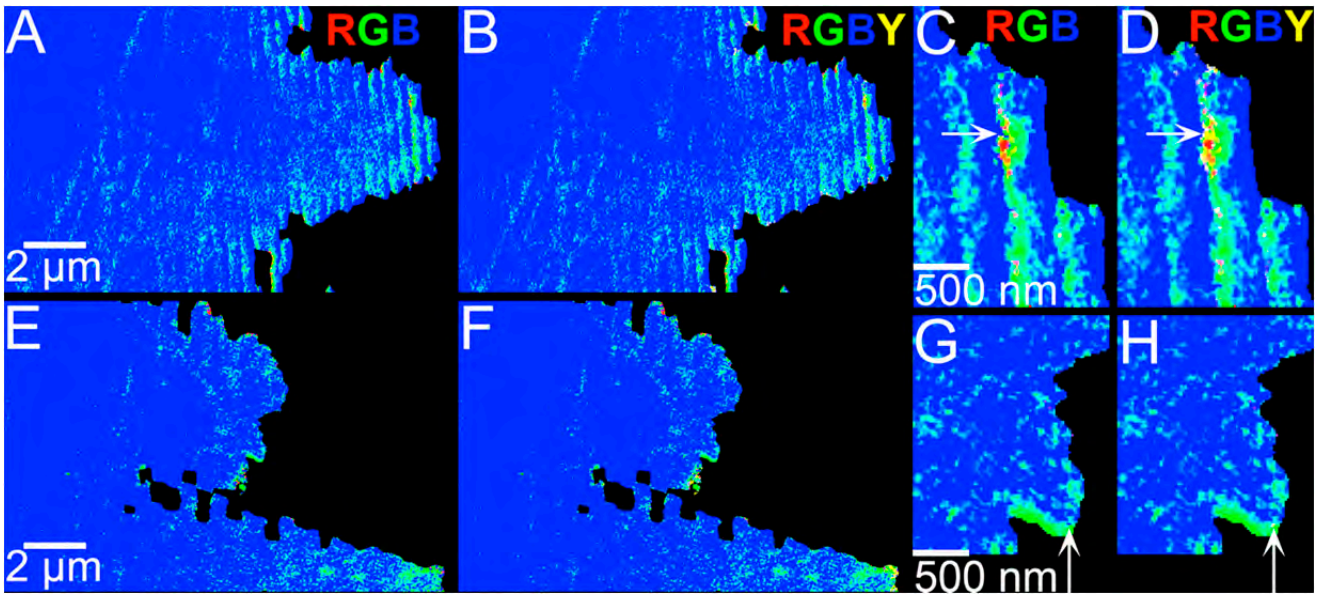

Figure S3. We address the question of whether doing the component mapping in nacre with or without proto-aragonite (pAra) affects the results by calculating the component map of the same nacre regions with 3 components (RGB = ACC-H_2O, ACC, Aragonite) or 4 components (RGBY, same as RGB plus pAra, with pAra displayed in Yellow). The result is striking: there are almost no pixels that map as pAra in nacre. The few we could observe (arrows in C, D and G, H) are localized at the interface of ACC (green) and aragonite (blue) regions, which is consistent with the fact that the pAra spectrum is intermediate between ACC and Ara, as shown in Figure 1F. Hence it is plausible that ACC, or Ara, or ACC+Ara could be misinterpreted as pAra in high-noise locations. The pAra pixels found in nacre are so few that it is safer to disregard them as noise or experimental error. In coral, however, there is a lot of pAra.

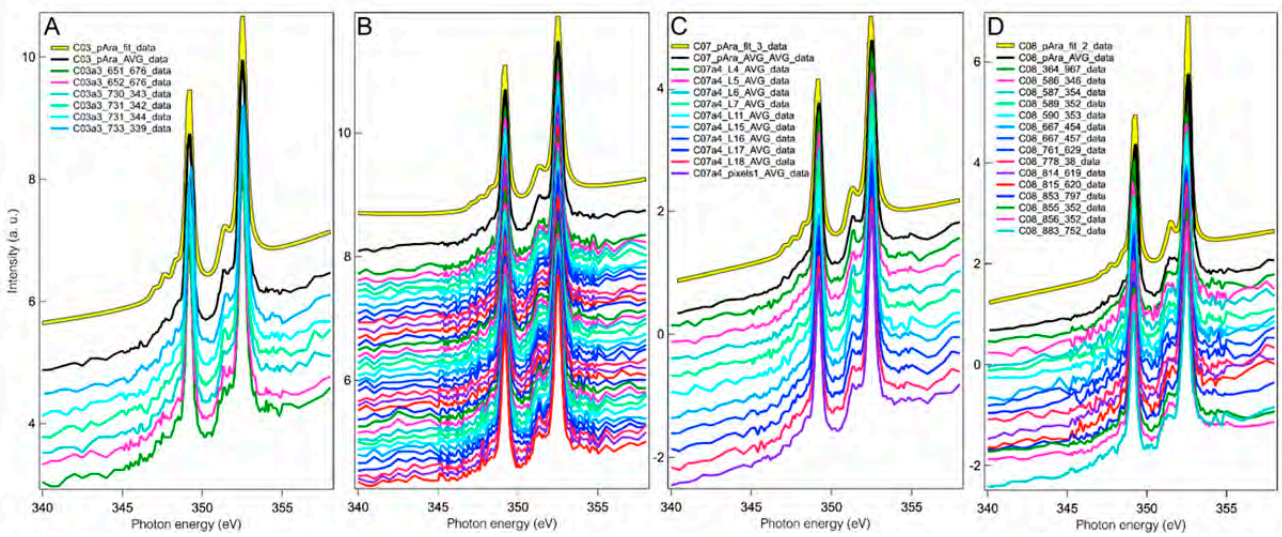

Figure S4. The proto-aragonite spectra obtained from single-20nm-pixels in coral. (A-D) Ca spectra acquired from 4 distinct Ca movies at centers of calcification in a *Madracis sp.* coral. Figure 2 shows a vertical band with many centers of calcification. Each single spectrum was extracted from a pixel displaying more than 80% pAra in component mapping. (A) Six spectra from one movie (C03) are displayed in colors, with pixel coordinates in their labels, their average spectrum in black, and peak fitting of the average in yellow outlined in black. (B) Thirty-six spectra from a second movie (C04), with labels omitted to avoid crowding of the spectra, again averaged in black and peak-fitted in yellow. (C) One hundred spectra were extracted from a third movie (C07), along specific lines. Instead of showing all 100 here we display the average spectrum for each line of pixels, then the average of all these averages in black, and its peak-fitting in yellow. (D) Sixteen spectra extracted from single pixels in a fourth movie (C08), averaged in black, peak-fitted in yellow.
(A-D) The peak-fitted yellow spectra at the top of each set of spectra were averaged to provide the pAra reference spectrum displayed in Figures 1C and 1F, and distributed in the various nacre and coral samples where yellow pixels are observed in component maps (Figure 1B, S1, S3).

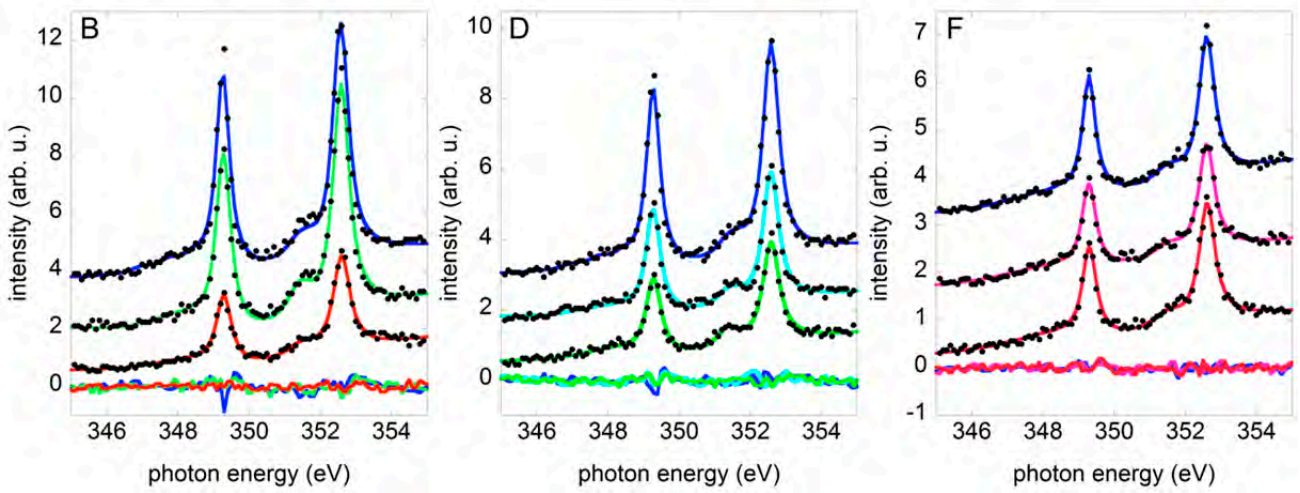

Figure S5. First, last, and intermediate spectra from panels B, D, and F of Figure 4 in the main text. The raw data (black dots) are fitted (solid curves) using a linear combination of the three component spectra, ACC-H_2O, ACC, and aragonite. In the linear combination the weight of each component is the percentage obtained from the component mapping and displayed in Figure 4, panels B, D, and F. The color assigned to each linear combination is the same as in Figure 3. Raw data and fits are overlapped, and their differences, termed residuals, are displayed at the bottom of each set of spectra, also color coded as in the linear combination and in Figure 4. All residuals exhibit only randomly distributed noise, thus demonstrating the reliability of the component mapping method.

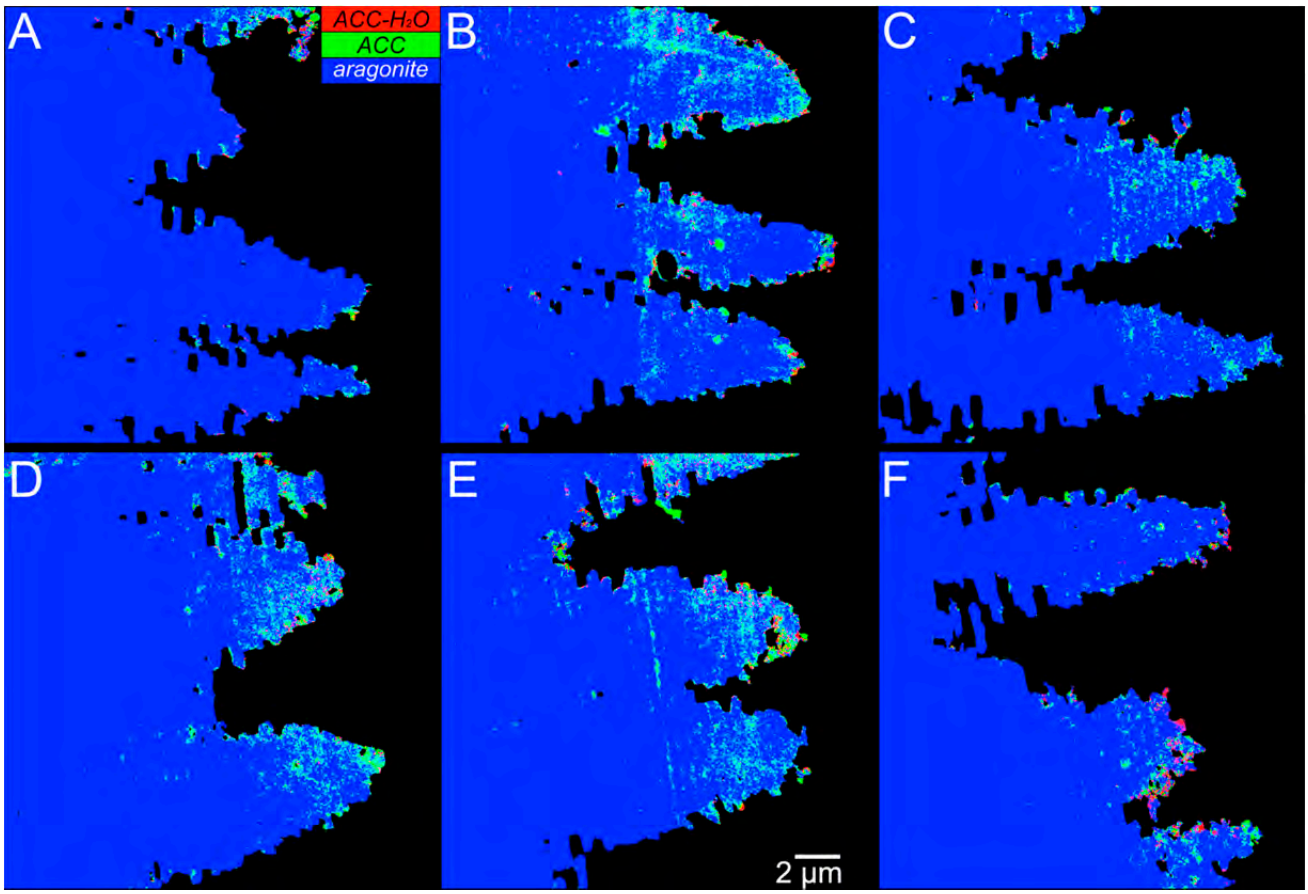

Figure S6. RGB component maps of the first movies on six different forming nacre areas. In all maps, green pixels are more common than red pixels. Y pAra was omitted as it does not occur in nacre, as shown in Figure S3, and four components slow down the calculation time for component maps from ~3+ hours to ~4+ hours. (These are the times it takes if one runs a single Igor experiment at once. If one runs multiple experiments (up to 16 can run at once on a PC, it takes 4.5 and 5.5 hours with 3 and 4 components, respectively.) Analysis of the same regions presented here produces nearly identical maps when using 3 or 4 components: pAra only occurs in 10 or fewer pixels per image (out of 10^6), and can therefore be safely excluded.

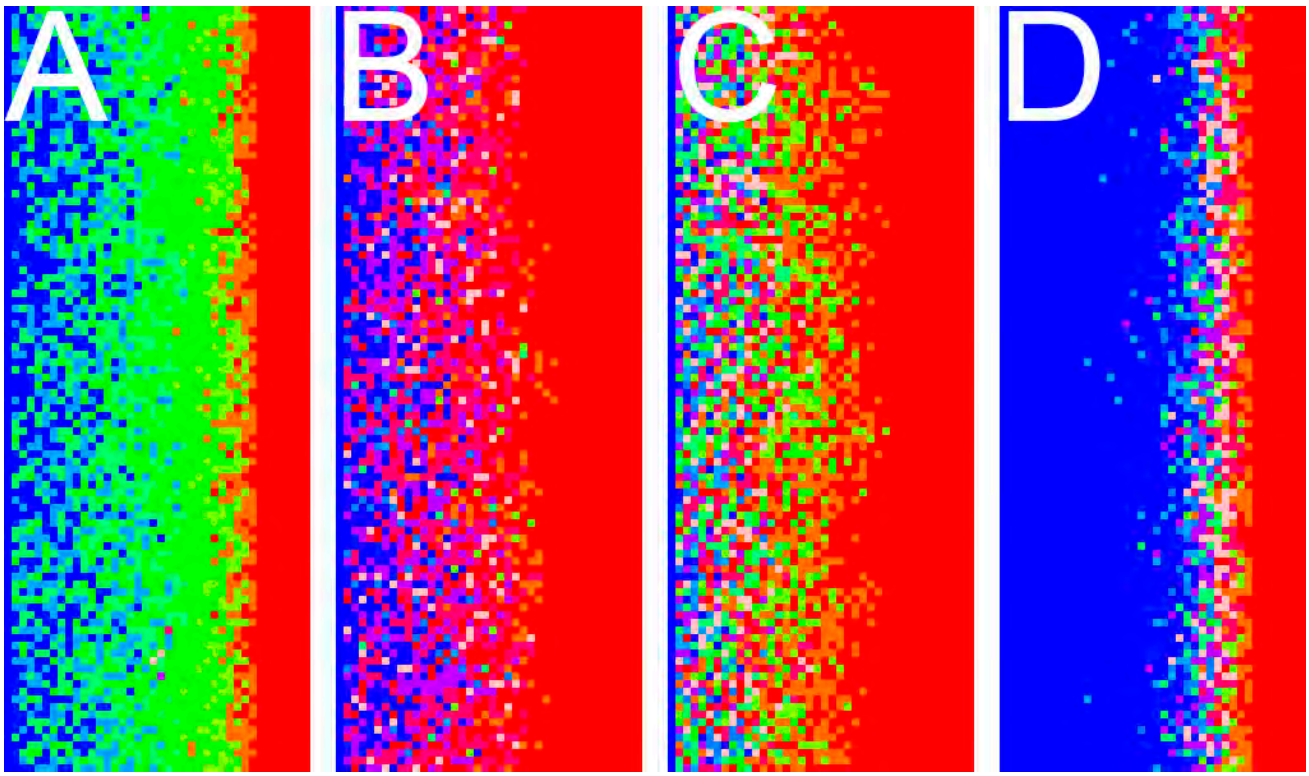

Figure S7. Computer-generated simulations showing each possible combination of slow and fast for the R-to-G and G-to-B transitions: (A) fast R-G, slow G-B; (B) slow R-G, fast G-B; (C) slow R-G, slow G-B; (D) fast R-G, fast G-B. The images shown are 2D slices through a 3D model system.

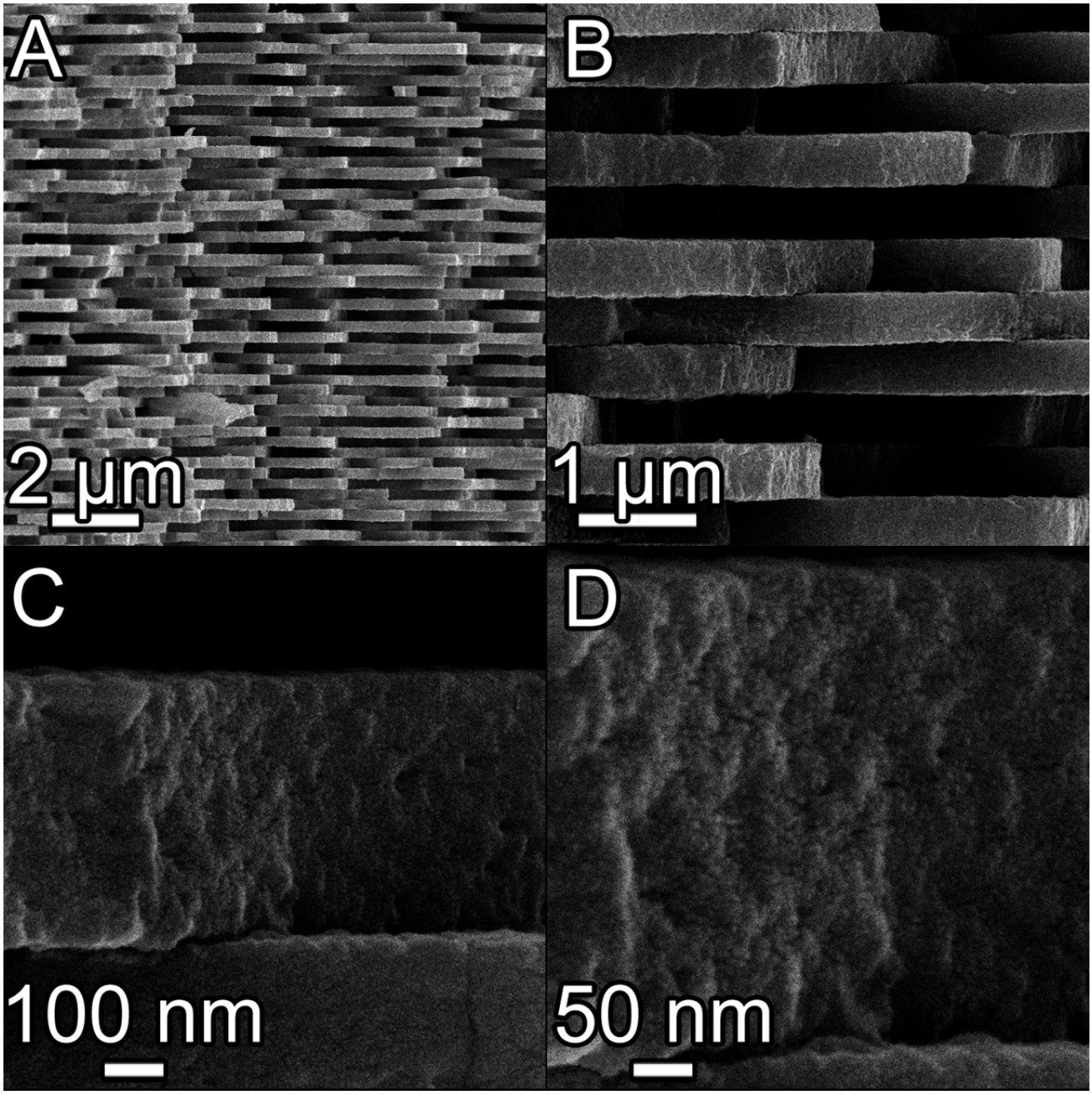

Figure S8. SEM images of nacre in a cryo-fractured *Haliotis rufescens* shell. (A, B, C, D) Increasing magnification micrographs of the same fractured nacre surface. Notice nanoparticles that were presumably amorphous when they aggregated and filled space completely, and then subsequently transformed into crystalline aragonite. Nacre tablets are not porous, they are space-filling, but they break with this nanoparticulate fracture figure, because crystal defects accumulate at the surface of nanoparticles, and therefore that is where they most likely fracture [12,13].

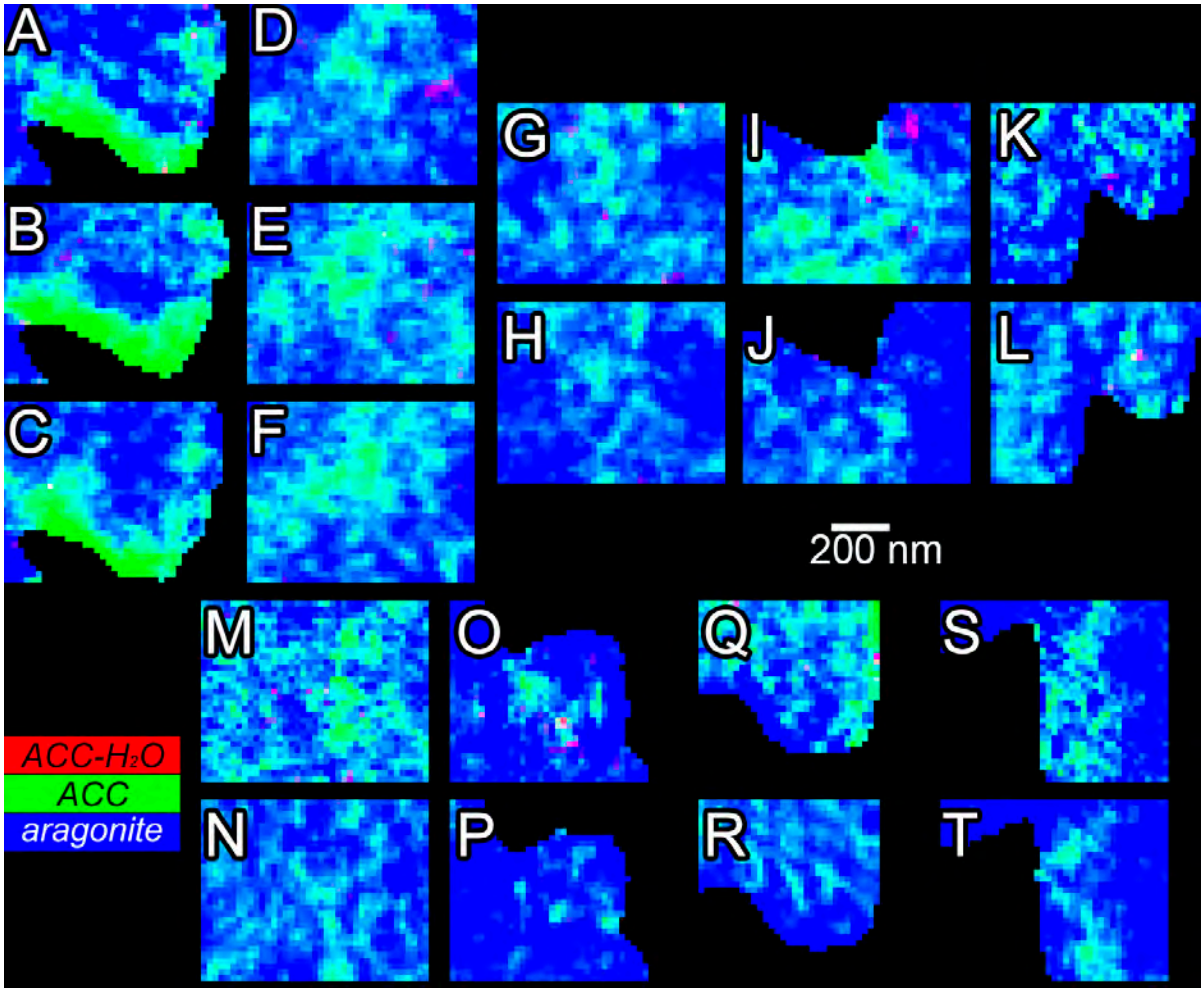

Figure S9. Component maps of small regions from three sequential movies on two different areas (A-C, D-F) and from two sequential movies on seven different areas (G-H, I-J, K-L, M-N, O-P, Q-R, S-T) from two shells, used to assess the effect of radiation damage. Some repeat movies produce identical results, others differ. When they differ, e.g. D and E, and E and F, radiation damage transforms red pixels into green pixels, and green pixels into blue pixels, thus it accelerates the phase transitions that would spontaneously occur.

Table S1

		ACC-H_2O nacre	ACC nacre	proto-aragonite	nacre aragonite	geologic aragonite	calcite spicules
polynomial	p0	-2.6462E-02	-2.7049E-02	-2.5548E-02	-2.4294E-02	-3.3546E-02	-6.0801E-02
	p1	1.0404E-03	-1.1280E-03	1.4474E-03	-2.5749E-03	-2.9982E-03	-8.7260E-03
	p2	6.1740E-04	6.6010E-04	7.0421E-04	6.3892E-04	5.0130E-04	3.2349E-04
	p3	2.7446E-05	4.9058E-05	2.4644E-05	6.1592E-05	4.6079E-05	6.7200E-05
peak 1	Amplitude	0.88	0.81	0.91	0.79	0.75	0.97
	Position	352.6	352.6	352.6	352.6	352.6	352.6
	Width	0.62	0.56	0.61	0.51	0.48	0.64
peak 2'	Amplitude	-	-	-	0.05	0.06	-
	Position	-	-	-	351.6	351.64	-
	Width	-	-	-	0.60	0.60	-
peak 2	Amplitude	0.12	0.18	0.18	0.03	0.05	0.27
	Position	351.5	351.4	351.5	351.3	351.2	351.4
	Width	1.00	0.65	0.74	0.60	0.60	0.57
peak 3	Amplitude	0.62	0.60	0.72	0.63	0.56	0.82
	Position	349.3	349.3	349.3	349.3	349.3	349.2
	Width	0.57	0.52	0.55	0.46	0.43	0.59
peak 4'	Amplitude	-	-	0.06	0.04	0.05	-
	Position	-	-	348.4	348.5	348.5	-
	Width	-	-	0.58	0.55	0.54	-
peak 4	Amplitude	0.31	0.27	0.08	0.06	0.06	0.26
	Position	348.0	348.1	347.8	347.8	347.8	347.9
	Width	2.10	1.76	0.78	0.80	0.85	0.81
peak 4''	Amplitude	-	-	0.04	0.03	0.02	-
	Position	-	-	347.12	347.0	347.14	-
	Width	-	-	0.70	0.76	0.50	-
arctan 1	Amplitude	0.04	0.04	0.02	0.02	0.02	0.04
	Position	352.5	352.5	352.5	352.5	352.5	352.5
	Width	0.40	0.40	0.40	0.40	0.40	0.40
arctan 2	Amplitude	0.09	0.09	0.05	0.05	0.05	0.09
	Position	351.0	351.0	351.0	351.0	351.0	351.0
	Width	0.40	0.40	0.40	0.40	0.40	0.40

Table S1. Best-fit coefficients for the six peak-fitted spectra in Figure 3, plus sea urchin spicules spectra in Figure 1: the four reference spectra used for component mapping of nacre and coral, geologic aragonite, sea urchin spicule ACC-H_2O, ACC, and calcite. The background is a third-order polynomial with p0, p1, p2, p3 coefficients. Peaks are all Lorentzian curves, and ionization potentials are arctangents. All of these numbers were free fit parameters, except for the arctangents, which were held fixed in position and width. Peak Amplitude is the area under the Lorentzian curve; peak Position, expressed in eV, is the binding energy or photon energy position of each Lorentzian or arctangent center; the peak or arctangent width is also expressed in eV. Peak position shifts of ±0.1 eV are comparable with the spectrum energy step used, and are therefore not significant.

Table S2

	percent ACC1	percent ACC2	percent aragonite
R-G-B	0%	0%	100%
R-G-B	0%	0%	100%
R-G-B	0%	0%	100%
R-G-B	0%	27%	73%
R-G-B	0%	27%	73%
R-G-B	21%	51%	28%
R-G-B	23%	56%	21%
R-G-B	30%	52%	18%
R-G-B	34%	49%	17%
R-G-B	39%	50%	11%
R-G-B	56%	37%	7%
R-G-B	67%	29%	4%
R-G-B	69%	23%	7%
R-G-B	85%	11%	4%
G-C-B	0%	0%	100%
G-C-B	0%	0%	100%
G-C-B	0%	12%	88%
G-C-B	0%	53%	47%
G-C-B	0%	51%	49%
G-C-B	0%	46%	54%
G-C-B	0%	51%	49%
G-C-B	0%	65%	35%
G-C-B	0%	76%	24%
G-C-B	0%	82%	18%
G-C-B	1%	91%	8%
R-M-B	0%	0%	100%
R-M-B	0%	0%	100%
R-M-B	0%	9%	91%
R-M-B	28%	0%	72%
R-M-B	58%	0%	42%
R-M-B	73%	0%	27%
R-M-B	74%	0%	26%
R-M-B	76%	0%	24%
R-M-B	81%	0%	19%

Table S2. Percentages of spectral components for all the spectra in Figure 4. The rows highlighted in yellow correspond to the spectra in Figure S5.

References

(1) De Stasio, G.; Frazer, B. H.; Gilbert, B.; Richter, K. L.; Valley, J. W. *Ultramicroscopy* **2003**, *98*, 57.
(2) Gilbert, P. U. P. A. In *Biomineralization Handbook, Characterization of Biominerals and Biomimetic Materials*; DiMasi, E., Gower, L. B., Eds.; CRC Press: Boca Raton, FL, 2014, p 135.
(3) Gilbert, P. U. P. A.; Metzler, R. A.; Zhou, D.; Scholl, A.; Doran, A.; Young, A.; Kunz, M.; Tamura, N.; Coppersmith, S. N. *J Am Chem Soc* **2008**, *130*, 17519.
(4) Olson, I. C.; Kozdon, R.; Valley, J. W.; Gilbert, P. U. P. A. *J Am Chem Soc* **2012**, *134*, 7351–7358.
(5) Leung, B. O.; Hitchcock, A. P.; Cornelius, R. M.; Brash, J. L.; Scholl, A.; Doran, A. *Journal of Electron Spectroscopy and Related Phenomena* **2012**, *185*, 406.
(6) Doran, A.; Church, M.; Miller, T.; Morrison, G.; Young, A. T.; Scholl, A. *J Electr Spectrosc Rel Phenom, special issue on Photoelectron microscopy, Time-resolved pump-probe PES* **2012**, *185*, 340.
(7) Gong, Y. U. T.; Killian, C. E.; Olson, I. C.; Appathurai, N. P.; Amasino, A. L.; Martin, M. C.; Holt, L. J.; Wilt, F. H.; Gilbert, P. U. P. A. *Proc Natl Acad Sci USA* **2012**, *109*, 6088.
(8) DeVol, R. T.; Metzler, R. A.; Kabalah-Amitai, L.; Pokroy, B.; Politi, Y.; Gal, A.; Addadi, L.; Weiner, S.; Fernandez-Martinez, A.; Demichelis, R. *J Phys Chem B* **2014**, *118*, 8449.
(9) GG-Macros http://home.physics.wisc.edu/gilbert/software.htm **2015**.
(10) Hephaestus http://cars9.uchicago.edu/~ravel/software/doc/Athena/mobile/hephaestus.html **2015**.
(11) Mucal http://csrri.iit.edu/mucal.html **2015**.
(12) Gal, A.; Kahil, K.; Vidavsky, N.; DeVol, R. T.; Gilbert, P. U.; Fratzl, P.; Weiner, S.; Addadi, L. *Adv Funct Mater* **2014**, *24*, 5420.
(13) Gal, A.; Weiner, S.; Addadi, L. *CrystEngComm* **2015**, *17*, 2606.